

MODELING THE MELT POOL OF THE LASER SINTERED Ti6Al4V LAYERS WITH GOLDAK'S DOUBLE-ELLIPSOIDAL HEAT SOURCE

E. Soylemez*

*Department of Mechanical Engineering, Faculty of Engineering, Marmara University, Goztepe
Kadikoy, 34722, Istanbul, Turkey

Abstract

Selective laser melting process has been widely studied to elucidate the effects of process parameters (laser speed, laser power, scan strategy, hatch distance, layer thickness, etc.) on the manufactured parts. Experimental and numerical modeling studies have been investigating the melt pool shapes of the laser sintered layers to correlate the melt pool geometry with the part quality. Although modeling results agree with the experiments, the melt pool cross-section may form key holing rather than semi-circular shape due to Marangoni effect, recoil pressure, and sudden evaporation for some process parameters combinations. To accurately model the melt pool depth, this study proposes a finite element analysis (FEA) model that simulates the laser source as the Goldak's double-ellipsoidal heat power density model. Single bead experiments of Ti6Al4V were conducted within the processing range of laser sintering system with the 400 W laser, and these experimental results allowed to verify simulated FEA results.

Keywords: Finite Element Analysis, Selective Laser Melting, keyhole, process map

Introduction

Selective laser melting (SLM) process is the most common metal additive manufacturing (AM) method owing to the recent technological advancements in lasers, expired intellectual properties of the technique, electronic equipment cost reductions and further controlling capabilities in the recent years. Precise laser source provides manufacturing of the high quality parts. However, process parameters (laser speed, laser power, laser diameter, hatch distance, layer thickness, ambient temperature, etc.) [1], the scan strategies [2], and the powder characteristics relation to the resulting part should be considered thoroughly.

Heat transfer, phase transition, laser beam energy-material interaction, surface tension induced melt pool motion, material vaporization and ejection, and chemical reactions are the observed physical incidents at the SLM process [3]. Controlling these physical phenomena with process parameters is crucial for the production part quality. For instance, radial temperature distribution from the center of the beam where the greatest temperature results, causes a surface tension variation. Thus, mass transfer develops in the melt pool due to surface tension increment while temperature decreases, known as Marangoni effect [4]. Another defect is called keyholing that appears when the melt pool liquid scatter around due to surface tension variations under the beam or rapid evaporation under the beam region, which causes a recoil pressure that provides further penetration of the melt material into the preceding layers [5]. If keyhole is dominant with larger penetration size compared to laser track on the surface, the thermal transfer mechanism is called as keyhole mode [5]. If the thermal conduction is the main melt pool evolution reason, it is called as conductive mode. Keyhole penetration causes voids under the surface due to entrapped air during the cooling of the melt pool.

To understand the physics and foresee the process behavior, researchers have simulated the process numerically [6, 7]. Due to the computational power limitations, the different levels of scales have been simulated [6, 7]. These are simulating the powder melting physics inside the melt pool [8], simulating the temperature distributions to measure the melt pool sizes [9], and simulating the parts in macro-scale coupled by thermal-mechanical relationships to check the distortions and stresses built up during the process [10–12]. While powder scale models present the details in the melt pool, simulation time would be impractical for part scale simulations. One step coarser models that focuses on the melt pool geometry predictions can be employed in the part-scale models with multiple-scale approaches besides to adaptive meshing techniques. Therefore, correlating the melt pool geometry SLM process can be a useful tool. For instance, the melt pool length to depth ratio helps to estimate microstructure grain types of the alloy [13], melt pool length to width variation relates to grain orientation [14] and track stability [3], and melt pool depth to width ratio can define the key hole transition [15].

This study established a numerical model that can match the melt pool geometries observed in the experiments between 50 W and 400 W laser powers. Ti6Al4V is the chosen material because it is one of the most frequently used material in aerospace and biomedical industries with high waste cost. It provides high mechanical strength, high creep resistance, high corrosion resistance, high fatigue strength, low relative density, and biocompatibility. Single bead [16–18] and raster scan [19] melt pool investigations have been conducted for Ti6Al4V. However, finite element analysis (FEA) studies in the literature have not distinguished the key hole mode of the SLM. In this study, empirical fit equation was produced to shape the volumetric heat source as a function of the laser power and velocity. This calibrated heat source can be utilized for part-scale models to check if any defective region occurs due to keyholing.

Methods

Experiments

Single bead experiments were run by EOS M290 with 400 W peak laser power at 1060 nm wavelength with continuous wave radiation. Base square plate with 132 mm side length and 5 mm thickness was ground to reach below 5 μm flatness. 44 different laser power and velocity combinations of the heat source shown in Table 1 were exposed to the experimental plane. Two experimental sets, no-powder case and powder case, were conducted. No-powder case included the 44 single bead lines at 40 mm length on the preheated Ti6Al4V plate. Powder case repeated the experiment with 30 μm Ti6Al4V powder layer provided by EOS on the plate. Before laser scanning, ambient temperature maintained at 35 °C and oxygen concentration in the chamber dropped to <0.1%.

Table 1 Investigated laser power and velocity parameters.

Power (W)	50, 100, 200, 250, 300, 350, 370
Velocity (mm/s)	200, 400, 800, 1200, 1600, 2000, 2400, 2800, 3200

After running the experiments, single bead width measurements were conducted. Later, plates were cut by using an electrical discharge machining (EDM) process in which three different samples from the center location of the single bead lines and 5 mm aside from the center to either direction were collected. These samples mounted with Bakelite black by applying a hot mounting press. Then, the samples were sanded with 240-grit sandpaper and 800-grit sandpaper. After that,

the samples were polished with alumina, 9 μm diamond, 1 μm diamond, and 0.03 μm colloidal silica, respectively. Finally, the samples were etched with Kroll's reagent etchant (91 ml water, 6 ml HNO_3 , and 3 ml HF) for ~ 30 s to observe the melt pool area details under optical microscope.

Numerical Model

3D finite element analysis (FEA) model was built up to simulate experimental single line scans for both no-powder and powder cases. Autodesk Netfabb Local Simulation 2018.2 software was used to conduct the FEA analysis. Simulation substrate size was 4.2 mm x 3.9 mm x 4 mm in x , y and z directions, respectively. 30 μm top layer was also added to be able to define the powder layer. Powder layer elements were defined by the powder material properties. When the temperature of the element reached the melting temperature, the element's material properties were converted to the solid structure material properties. Initial, ambient and bottom face nodal temperatures were set to 35 $^\circ\text{C}$. To reduce the computational time, elements resolution was biased towards to middle of the y axis in which the laser source moved along that axis in positive x direction on the top face. Therefore, melt pool steady state temperature profile was gained. Figure 1 shows the cross-sectional view of the temperature contour plots. Figure 1(a) shows the cross-section in the x - z plane where the melt pool tail and melt pool penetration can be examined. Figure 1(b) visualizes the melt pool cross-section area in y - z plane.

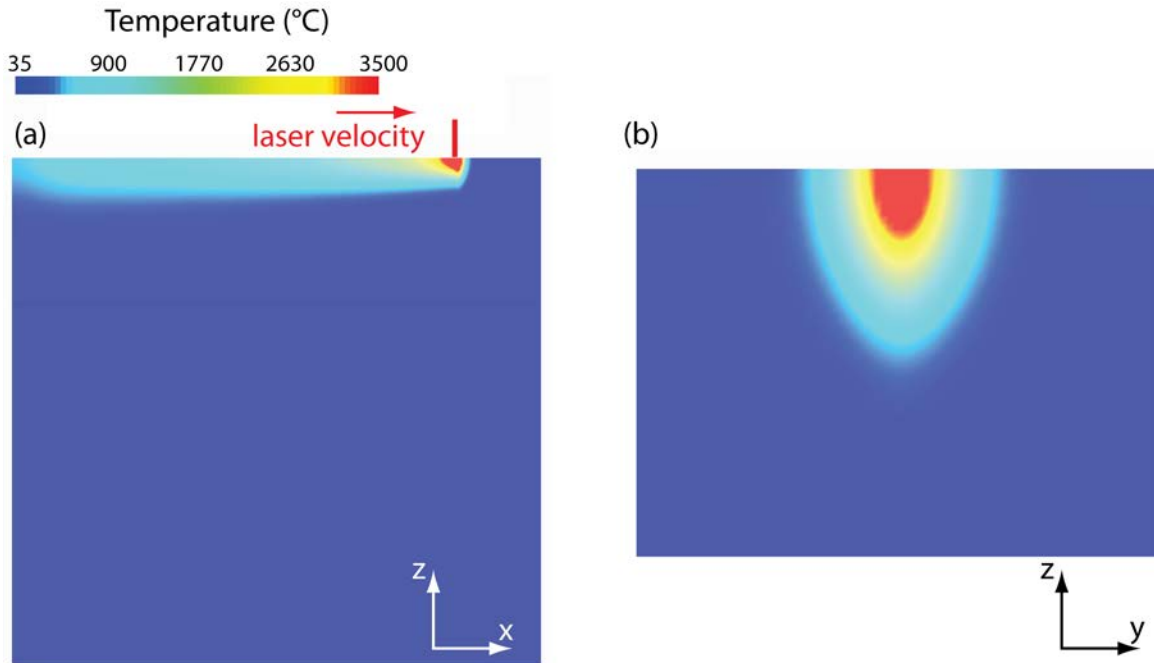


Figure 1. Sectional view of the temperature contour of the 3D thermal analysis: **(a)** x - z plane **(b)** y - z plane.

Material properties of Ti6Al4V alloy for heat transfer model were implemented. Table 2 displays the constant material properties in the simulation. Temperature dependent thermal properties [20], as shown in Figure 2, were also imported to the input file of the model. These thermal properties are for the solid structure. However, powder case simulations required different material properties to account the void behavior on the thermal transfer due to the insulation effect of the air. Top layer powder elements conductivity properties were scaled after running the equation as [16]

$$\frac{k_p}{k_s} = \frac{1-\varphi}{1-11\varphi^2} \quad (1)$$

where φ is void fraction, k_p is powder thermal conductivity, and k_s is the solid structure thermal conductivity. Void fraction value of 0.52 was used referring to [16], and 0.117 scaling factor was found. Also, powder density depends on the void fraction. Thus, that effect was implemented to the powder elements by scaling the specific heat of the powder elements in the simulation.

Table 2 Material properties used in the thermal simulations.

Property	Unit	Reference
Latent heat of fusion	286 J/g	Mills [20]
Solidus Temp	1620 °C	Fan and Liou [21]
Liquidus Temp	1650 °C	Mills [20]
Emissivity	0.65	Promoppatum et al. [16]
Convection Coefficient	12.7 W/m ² .K	Masoomi et al. [22]

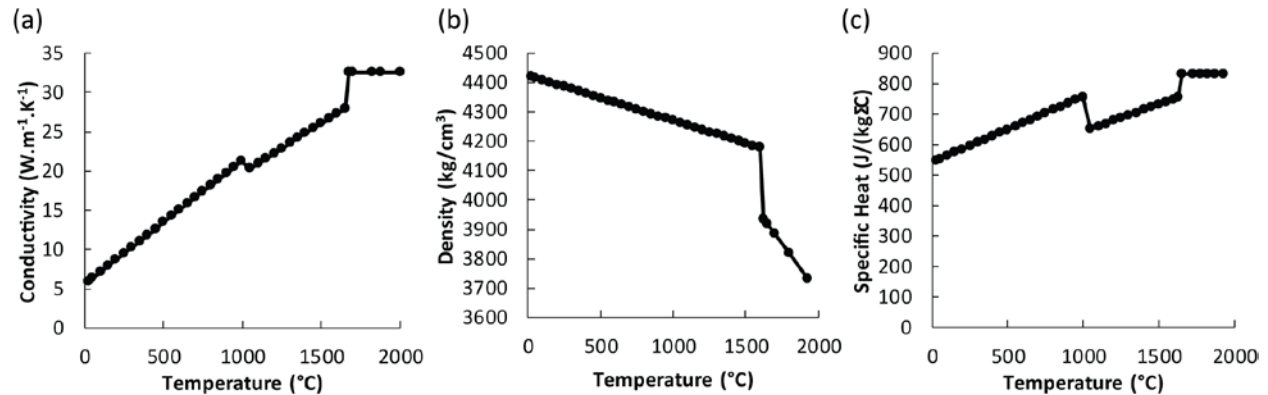


Figure 2. Temperature dependent (a) thermal conductivity, (b) density, and (c) specific heat of the Ti6Al4V alloy.

Another critical parameter in the simulations was laser absorption efficiency. Heat absorption efficiency can alter due to powder size, powder bulk density, laser wavelength, and material composition. Powder absorptivity is higher due to the penetration of the incident light by multiple reflections of the powder surfaces [23]. Boley et al. measured metal flat surface and powder absorption efficiencies by exposing 970 nm wavelength laser limited to 50 W cw laser power [24]. They presented 0.4 and 0.74 absorption efficiency values of Ti6Al4V alloy for a flat surface and the powder, respectively. Promoppatum et al. plotted the absorptivity curves as a function of the temperature in which 0.4 absorption efficiency for the solid at room temperature increased to ~0.7 near the melting temperature [16]. Thus, no-powder and powder case simulations used different absorption efficiencies. Software allowed using constant absorption efficiency. Therefore, 0.75 and 0.85 were selected to simulate no powder and powder cases, respectively. High values of absorption efficiencies can be explained by the compensation of not including temperature dependent absorption efficiencies and Marangoni effects inside the melt pool of the simulations.

Final detail of the numerical model is the heat source that allowed predicting the melt pool geometries realistically. Laser spot was modeled as a volumetric double ellipsoid heat source by the following equation developed by Goldak et al. [25]

$$Q = \frac{6\sqrt{3}P\eta}{abc\pi} e^{-\left[\frac{3x^2}{a^2} + \frac{3y^2}{b^2} + \frac{3(z+vt)^2}{c^2}\right]} \quad (2)$$

Here, a , b , and c are the parameters that shapes the volumetric ellipsoid. Local coordinates were represented by x , y , and z . P is the laser power, and η is the absorption efficiency. For best representation of the moving melt pool, power density distribution was portioned out to 0.7 and 0.3 for double heat source of the back and front of the heat source, respectively [25]. Laser spot size was selected as 100 μm diameter consistent with EOS M290 specifications. In this study, a and b were kept constant as 1 that applies a Gaussian heat distribution on x - y plane. Intensity variation of the heat source in z direction depends on the parameter c . After various simulation iterations of the 24 different power and velocity combinations for no-powder case, c parameters were set to estimate the experimental melt pool geometry accurately.

Results and Discussion

Single Bead Tracks

Each single bead track was observed, and the images were captured from at least three different locations. After analyzing the no powder case, low energy density scanned tracks showed weak penetration. They can be distinguished by their tiny or none bumped region above the substrate. Figure 3(a) shows the topology image taken under the optical microscope. Stable tracks were defined when the track boundary lines are consistent along the scanned path and a consistent bead height was valid above the plate shown in Figure 3(b). On the other hand, unstable tracks as seen in Figure 3(c) formed droplets due to surface tension effects at high velocity combinations.

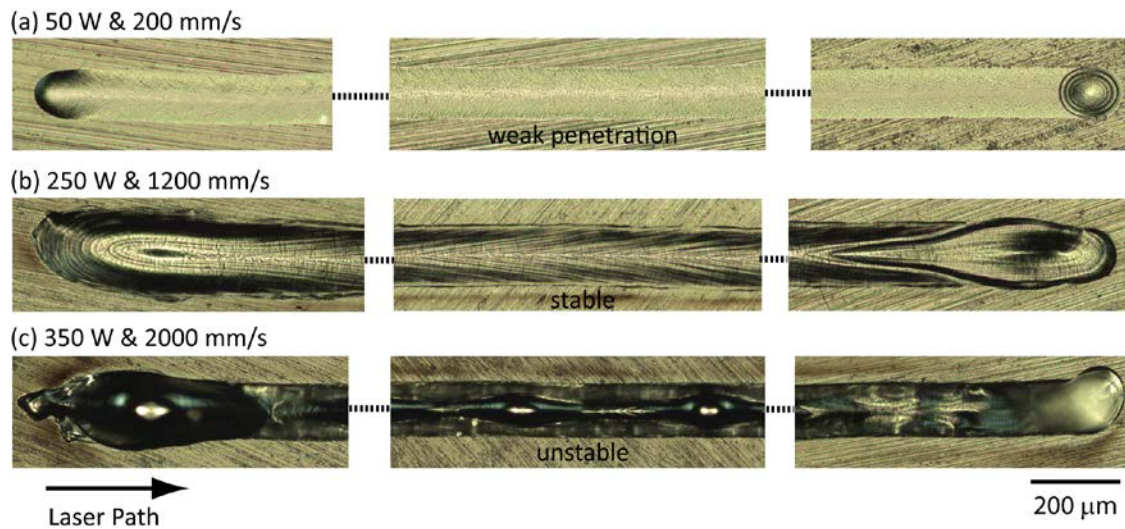


Figure 3. Top view of the distinctive single beads of no-powder case. **(a)** 50 W & 200 mm/s, **(b)** 250 W & 1200 mm/s, and **(c)** 350 W & 2000 mm/s.

For the powder case as seen in Figure 4, powder layer particles were attached to the bead tracks that were also evidenced by [26]. Powder alloy low-melting-point components could

create observed holes on the track [17]. Rapid evaporation under the beam region would also create holes on the tracks [5].

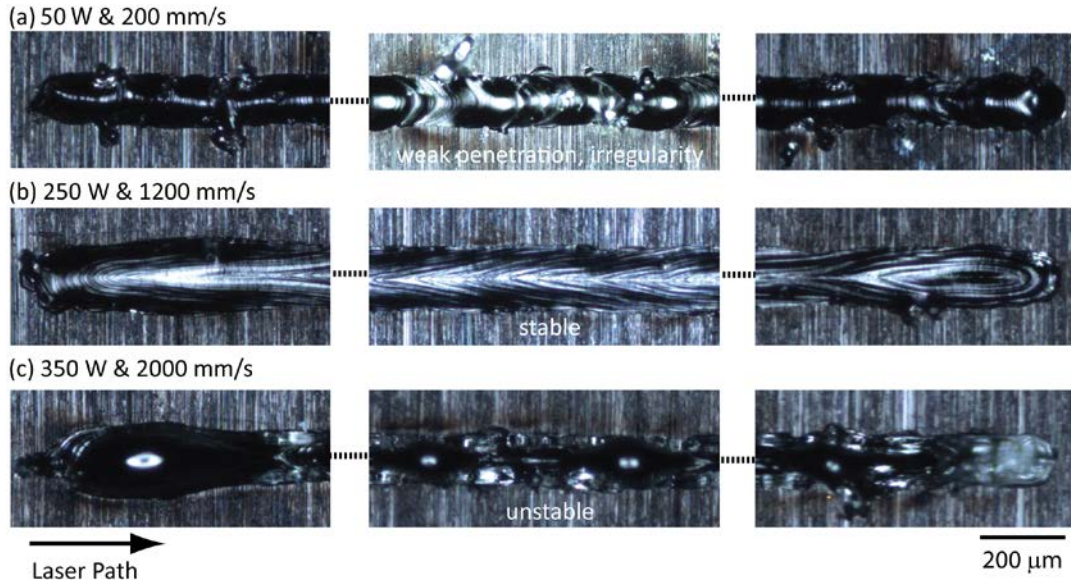


Figure 4. Top view of the distinctive single beads of powder case. **(a)** 50 W & 200 mm/s, **(b)** 250 W & 1200 mm/s, and **(c)** 350 W & 2000 mm/s.

Melt Pool Area

Details of the cross-section area of the melt pool helps to determine the reliable process parameter combinations to manufacture parts without flaws. Figure 5 shows the cross-section area of the melt pool, and it defines the melt pool depth, width, area, and bead height.

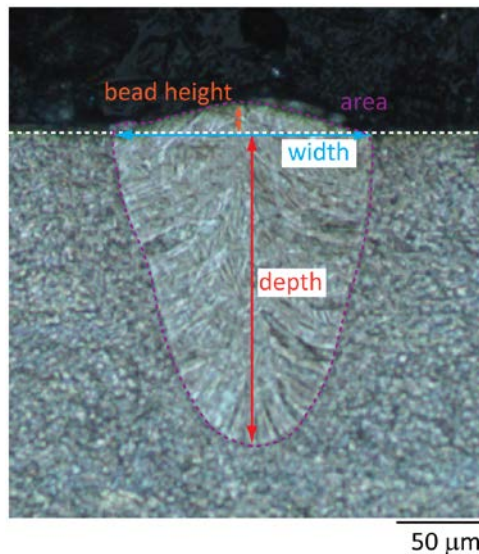


Figure 5. Single bead cross-section area and visual definitions of the melt pool size.

Cross-section areas of the single bead lines were examined under the microscope. Depending on the melt pool area and the observed defects, different process parameter

combinations were labeled as shown in Figure 6. If the melt pool depth/width ≤ 0.5 , melt pool area is defined as a semicircle. If the depth/width ≥ 0.5 , area is either called elliptical or keyhole. Keyhole can cause a pore defect. However, for smaller depth values, these defects were not present. Droplets due to balling effect can be observed as shown in Figure 6(c). In figure 7, same

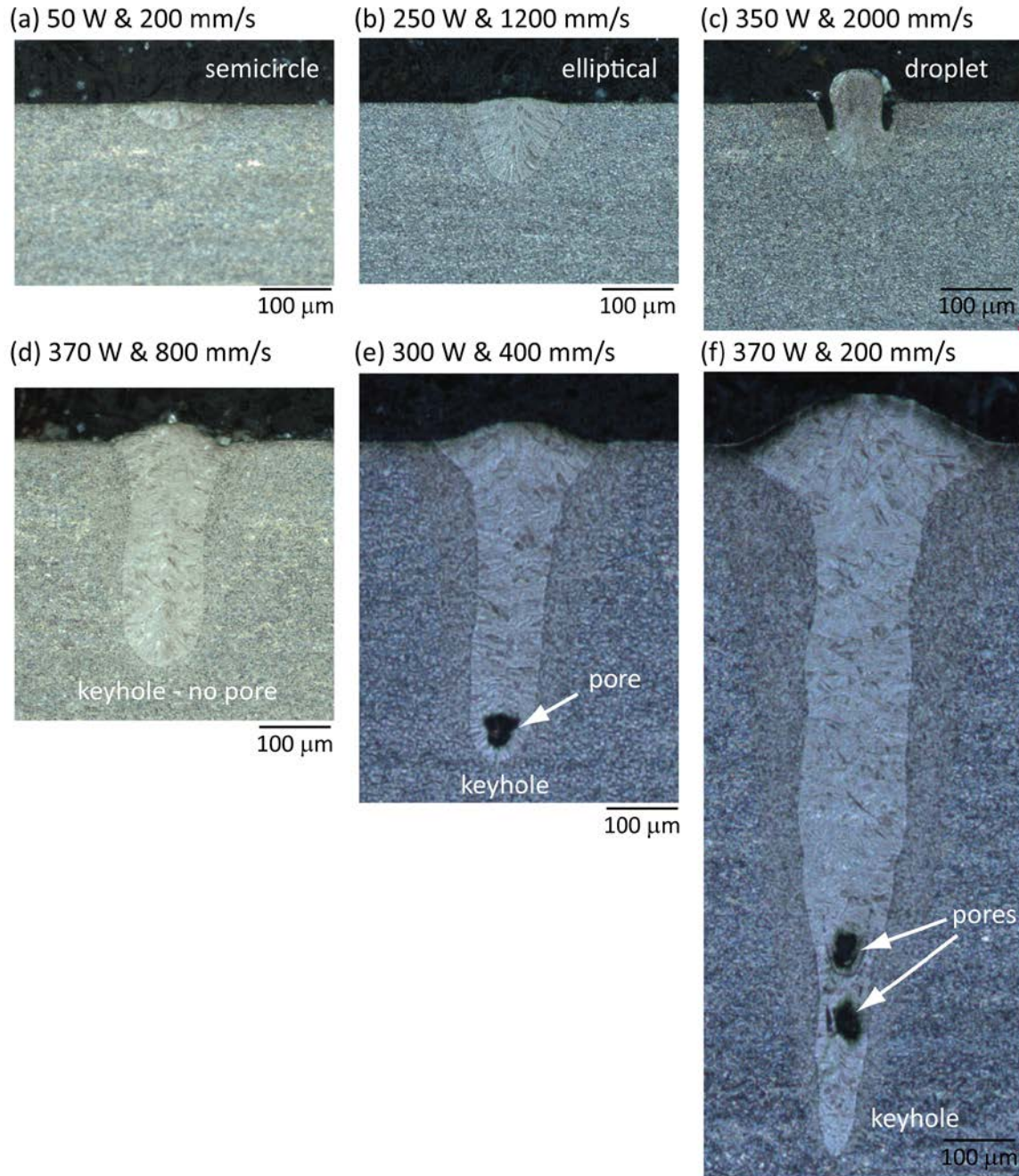


Figure 6. Various evolved melt pool profiles of multiple power and velocity combinations for the no-powder case.

process parameters cross-section area images can be seen for the powder case. The main difference is the larger bead height portion of the powder case melt pool areas. When

depth/width \leq 0.5, melt pool evolved due to the conductive mode. Opposite is the keyhole mode when the vaporization of the melt pool occurred [27].

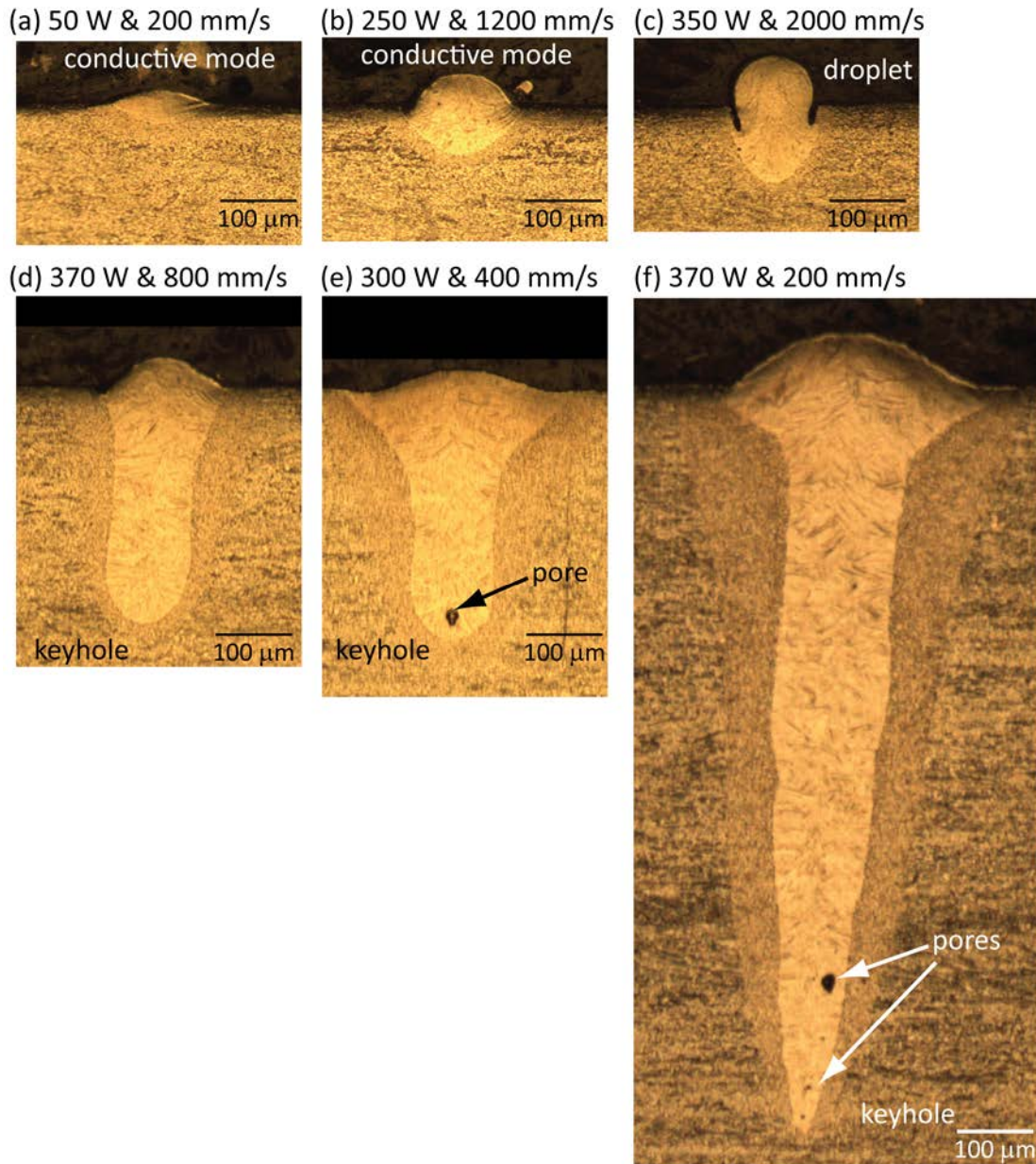


Figure 7. Various evolved melt pool profiles of multiple power and velocity combinations for the powder case.

Another important observation from the melt pool area investigations was related to the repeatability and reliability of the SLM system. Figure 8(a) shows the area for 200 W and 400 mm/s single bead, and on the right Figure 8(b) shows much smaller area at larger power of 250 W at the same speed. Gong et al. also reported this type of instability [17]. They explained it due to the possible laser fluctuations at high powers or high energy melt pool dynamics. However, I observed consistent cross-section areas for 44 parameters sectioned at three different locations at no-powder and powder cases except one single bead as seen in Figure 8(b). This suggests that

SLM system malfunctioning could initiate when executing a different parameter combination. Both studies happened to use EOS metal system. This might occur due to custom process parameter settings. However, it should be checked if these observations apply to the standard scanning conditions.

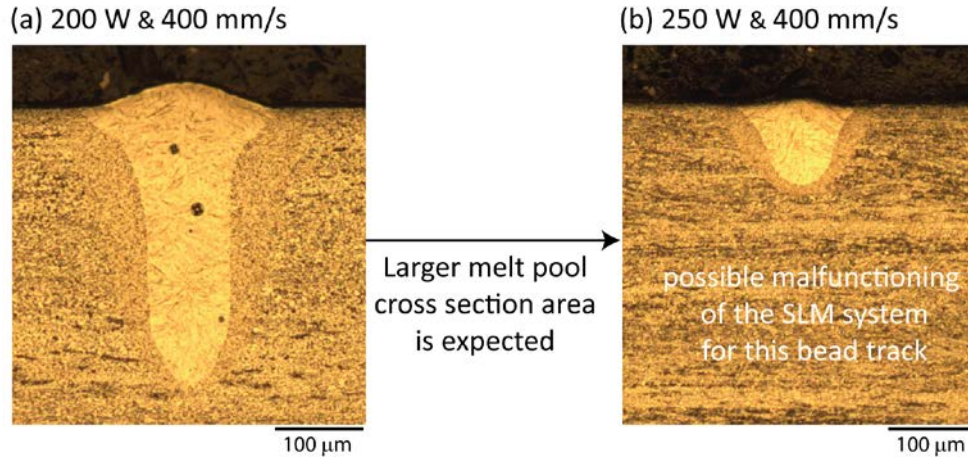


Figure 8. Melt pool cross-section area images of (a) 200 W & 400 mm/s and (b) 250 W & 400 mm/s. Significantly smaller melt pool area of (b) compared to (a) suggests that laser scanned the line at a lower energy density than the preset value.

Melt pool areas scanned at various power levels were plotted for 400 and 800 mm/s velocity combinations as a function of the laser power as seen in Figure 9. Circular and square markers show the average values of three different measurements of the experimental no-powder and powder cases, respectively. Percentage deviation from the mean for different process parameters varied from 1% to 36%. Powder case melt pool area values tend to be larger up to 21% compared to no-powder case. Blue markers correspond to 400 mm/s, and red markers that represent 800 mm/s bead lines have a smaller slope compared to lower velocity. Same trends are seen in the simulation results plotted with green and black marker for 400 mm/s and 800 mm/s, respectively. Since powder case laser absorption efficiency was set to a higher value compared to no-powder case and powder conductivity was scaled down, powder-case area simulation predictions were higher compared to no-powder consistent to the experimental results.

In addition to melt pool areas, melt pool depth and width values were also plotted as a function of the power for the powder case as shown in Figure 10 (Figure A1 for the no-powder case). Square markers represent experimental mean results, plus signs represent simulation values. Different colors mean different scan velocity. Figure 10 (b) and (d) zoomed in views to recognize high speed parameter results. Melt pool width values reach a steady state at 300 W. At higher scan speeds, the deviation of the melt pool width is not significant. On the other hand, melt pool depth suggests to have a linear increase as a function of the power. The slope of the increment drops as the velocity increases. Simulation agrees with the experimental trend. However, the values were slightly under-predicted.

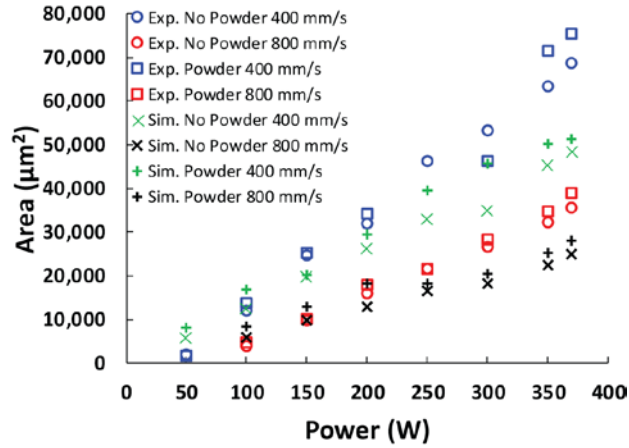


Figure 9. Melt pool area as a function of the power. Simulation, experiment, no-powder and powder case results are plotted with different type of marker types and color.

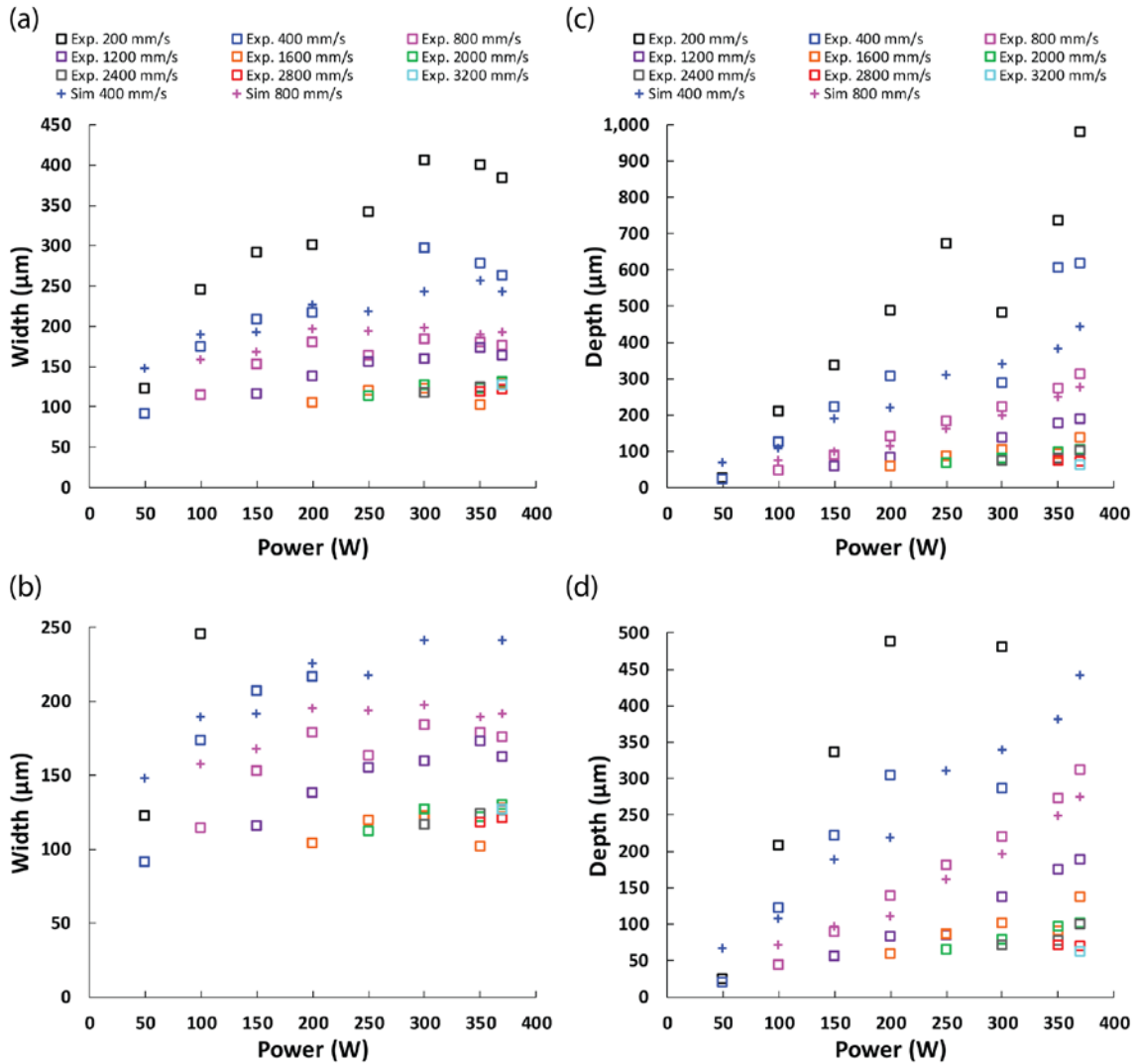


Figure 10. Melt pool width (a & b) and depth (c & d) as a function of the power for powder case. Simulation and experimental data are plotted with different markers. Different velocities are represented with different colors.

Process Control

Experimental observations were plotted in Figure 11 (Figure A2 no-powder case) for each process parameter combination of the powder case to establish a process map for SLM limited to 400 W laser source. Red markers correspond to keyhole melt pool areas with voids. Black markers are the combinations ending weak penetration. Orange markers where there were irregularities and balling defects on the track. Blue markers present asymmetric areas and distorted views of the track lines, but the track lines were still continuous. Therefore, it defines a transition region to the balling. In the welding literature, transition to balling region is also called as the pre-humping regime, and droplet region is called as the humping regime [5]. Green markers present safe parameters without voids at the cross-section area and show stable track from the top view.

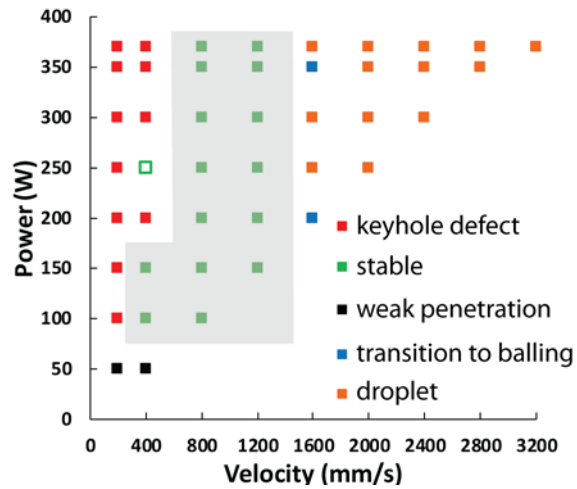


Figure 11. Single bead process map was plotted for Ti6Al4V with different colored markers. Powder layer thickness is 30 μm .

This process map is based on a single bead experiments of the powder case. However, during the part production, edge effects, hanging part sections, thin wall structures, scanning strategies etc. would end up with different melt pool geometries. This simulation study provided close approximations of the melt pool geometries. Therefore, accurate heat source modeling is expected to estimate keyhole defects due to the accumulated heat for a given geometry. After running the simulation of a part, nodal temperatures can be checked to compare depth to width ratios. According to the established process map, $\text{depth/width} \geq 1.2$ ends up with keyhole defect.

To be able to use the model for different process parameters, second order multivariate regression fit was conducted to find the c constant in the Goldak double heat source model by using Matlab R2017a. Conducted simulations process parameters were used as x_1 and x_2 , and c values of the simulations were also implemented. Resulting equation to estimate c was fit as

$$c = 0.5597 + 0.05311 P - 0.006504 V - 1.506 \times 10^{-5} P^2 - 2.914 \times 10^{-5} PV + 3.90310^{-6} V^2 \quad (3)$$

Here, P is power (W), and V is velocity (mm/s). With this equation, double volumetric heat source can be estimated for different process parameter combination accurately. Therefore, possible keyhole defects can be approximated, and design iterations and process conditions can

be improved for SLM. Equation 3 applies for Ti6Al4V. It has been understood that different material alloys can cause different depth/width ratios at different energy density levels [28]. Also, increasing the laser spot size helps to avoid keyhole formation [29]. As a future study, simulations can be run to compare SLM metal alloys experimental results, and an improved equation that also accounts the heat source diameter size and various metal alloys can be derived to find c .

Conclusions

Process parameters in the common SLM system power range were studied for no-powder case and 30 μm powder layer case. Process map was developed to present the power and velocity combinations effects on the part. Melt pool simulations were studied, and they predicted the melt pool geometries proximately. Goldak's double ellipsoidal volumetric heat source implementation was the key to accurately estimate the depth values due to the keyhole mode in the melt pool. Heat source predictions for different process parameter combinations for Ti6Al4V became possible with the empirical fit equation.

Acknowledgements

The author wishes to acknowledge Mert Coskun of the Fatih Sultan Mehmet University for performing the experiments and helping with the experimental planning. The author also would like to thank Michael Gouge and Sualp Ozel for their guidance on the Netfabb Simulation practices. The author also thanks to Semih Guven, a technical staff at the Marmara University for helping to polish the experimental samples, and Anil Gorkem Yekdes, an undergraduate student for helping the post-processing of the experimental and the numerical analysis data. The author gratefully acknowledges The Scientific and Technological Research Council of Turkey (TÜBİTAK) through Project No: 216M033.

References

1. Beuth J, Fox J, Gockel J, et al (2013) Process Mapping for Qualification Across Multiple

- Direct Metal Additive Manufacturing Processes Jack. Proc Solid Free Fabr Symp 655–665 . doi: 10.1017/CBO9781107415324.004
2. Mertens R, Clijsters S, Kempen K, Kruth J-P (2014) Optimization of Scan Strategies in Selective Laser Melting of Aluminum Parts With Downfacing Areas. J Manuf Sci Eng 136:061012 . doi: 10.1115/1.4028620
 3. Yadroitsev I, Gusarov A, Yadroitsava I, Smurov I (2010) Single track formation in selective laser melting of metal powders. J Mater Process Technol 210:1624–1631 . doi: 10.1016/j.jmatprotec.2010.05.010
 4. Anthony TR, Cline HE (1977) Surface rippling induced by surface-tension gradients during laser surface melting and alloying. J Appl Phys 48:3888–3894 . doi: 10.1063/1.324260
 5. Katayama S (2013) Handbook of Laser Welding, 1st ed
 6. Meier C, Penny RW, Zou Y, et al (2017) Thermophysical Phenomena in Metal Additive Manufacturing by Selective Laser Melting: Fundamentals, Modeling, Simulation and Experimentation. arxiv.org
 7. Megahed M, Mindt H-W, N'Dri N, et al (2016) Metal additive-manufacturing process and residual stress modeling. Integr Mater Manuf Innov 5:4 . doi: 10.1186/s40192-016-0047-2
 8. King W, Anderson AT, Ferencz RM, et al (2015) Overview of modelling and simulation of metal powder bed fusion process at Lawrence Livermore National Laboratory. Mater Sci Technol 31:957–968 . doi: 10.1179/1743284714Y.0000000728
 9. Soylemez E, Beuth JL, Taminger K (2010) Controlling Melt Pool Dimensions over a Wide Range of Material Deposition Rates in Electron Beam Additive Manufacturing. Proc 2010 Solid Free Fabr Symp 571–582
 10. Kundakcioglu E, Lazoglu I, Rawal S (2015) Transient thermal modeling of laser-based additive manufacturing for 3D freeform structures. Int J Adv Manuf Technol 1–9 . doi: 10.1007/s00170-015-7932-2
 11. Jamshidinia M, Kong F, Kovacevic R (2013) Numerical Modeling of Heat Distribution in the Electron Beam Melting ® of Ti-6Al-4V. J Manuf Sci Eng 135:061010 . doi: 10.1115/1.4025746
 12. Parry L, Ashcroft IA, Wildman RD (2016) Understanding the effect of laser scan strategy on residual stress in selective laser melting through thermo-mechanical simulation. Addit Manuf 12:1–15 . doi: 10.1016/j.addma.2016.05.014
 13. Gockel J, Beuth J, Taminger K (2014) Integrated control of solidification microstructure and melt pool dimensions in electron beam wire feed additive manufacturing of ti-6al-4v. Addit Manuf 1:119–126 . doi: 10.1016/j.addma.2014.09.004
 14. Dezfoli ARA, Hwang WS, Huang WC, Tsai TW (2017) Determination and controlling of grain structure of metals after laser incidence: Theoretical approach. Sci Rep 7:1–11 . doi: 10.1038/srep41527
 15. King WE, Barth HD, Castillo VM, et al (2014) Observation of keyhole-mode laser melting in laser powder-bed fusion additive manufacturing. J Mater Process Technol 214:2915–2925 . doi: 10.1016/j.jmatprotec.2014.06.005
 16. Promopattum P, Onler R, Yao SC (2017) Numerical and experimental investigations of micro and macro characteristics of direct metal laser sintered Ti-6Al-4V products. J Mater Process Technol 240:262–273 . doi: 10.1016/j.jmatprotec.2016.10.005
 17. Gong H, Christiansen D, Beuth J, Lewandowski JJ (2014) Melt Pool Characterization for Selective Laser Melting of Ti-6Al-4V Pre-alloyed Powder. In: Solid Freeform Fabrication Symposium. pp 256–267
 18. Karayagiz K, Elwany A, Tapia G, et al (2018) Numerical and Experimental Analysis of

- Heat Distribution in the Laser Powder Bed Fusion of Ti-6 Al-4 V. IISE Trans 5854:1–44 . doi: 10.1080/24725854.2018.1461964
19. Cheng B, Chou K (2015) Melt Pool Evolution Study in Selective Laser Melting. In: Solid Freeform Fabrication Symposium. pp 1182–1194
 20. Kenneth C. M (2002) Recommended values of thermophysical properties for selected commercial alloys. Woodhead Publishing
 21. Fan Z, Liou F (2012) Numerical Modeling of the Additive Manufacturing (AM) Processes of Titanium Alloy. Des Control Appl Mechatron Syst Eng 135–152 . doi: 10.5772/67458
 22. Masoomi M, Thompson SM, Shamsaei N (2017) Laser powder bed fusion of Ti-6Al-4V parts: Thermal modeling and mechanical implications. Int J Mach Tools Manuf 118–119:73–90 . doi: 10.1016/j.ijmachtools.2017.04.007
 23. Gusarov A V (2010) Radiation transfer in metallic-powder beds during laser forming. 451: . doi: 10.1070/QE2010v040n05ABEH013976
 24. Boley CD, Mitchell SC, Rubenchik AM, Wu SSQ (2016) Metal powder absorptivity : modeling and experiment. Appl Opt 55:6496–6500
 25. Goldak J, Chakravarti A, Bibby M (1984) A new finite element model for welding heat sources. Metall Trans B 15:299–305 . doi: 10.1007/BF02667333
 26. Zhao C, Fezzaa K, Cunningham RW, et al (2017) Real-time monitoring of laser powder bed fusion process using high-speed X-ray imaging and diffraction. Sci Rep 7:1–11 . doi: 10.1038/s41598-017-03761-2
 27. Scipioni Bertoli U, Wolfer AJ, Matthews MJ, et al (2017) On the limitations of Volumetric Energy Density as a design parameter for Selective Laser Melting. Mater Des 113:331–340 . doi: 10.1016/j.matdes.2016.10.037
 28. Elmer JW, Giedt WH, Eagar TW (1990) The Transition from Shallow to Deep Penetration during Electron Beam Welding. Weld J 1167–1176
 29. Francis Z (2017) The Effects of Laser and Electron Beam Spot Size in Additive Manufacturing Processes

Appendix A

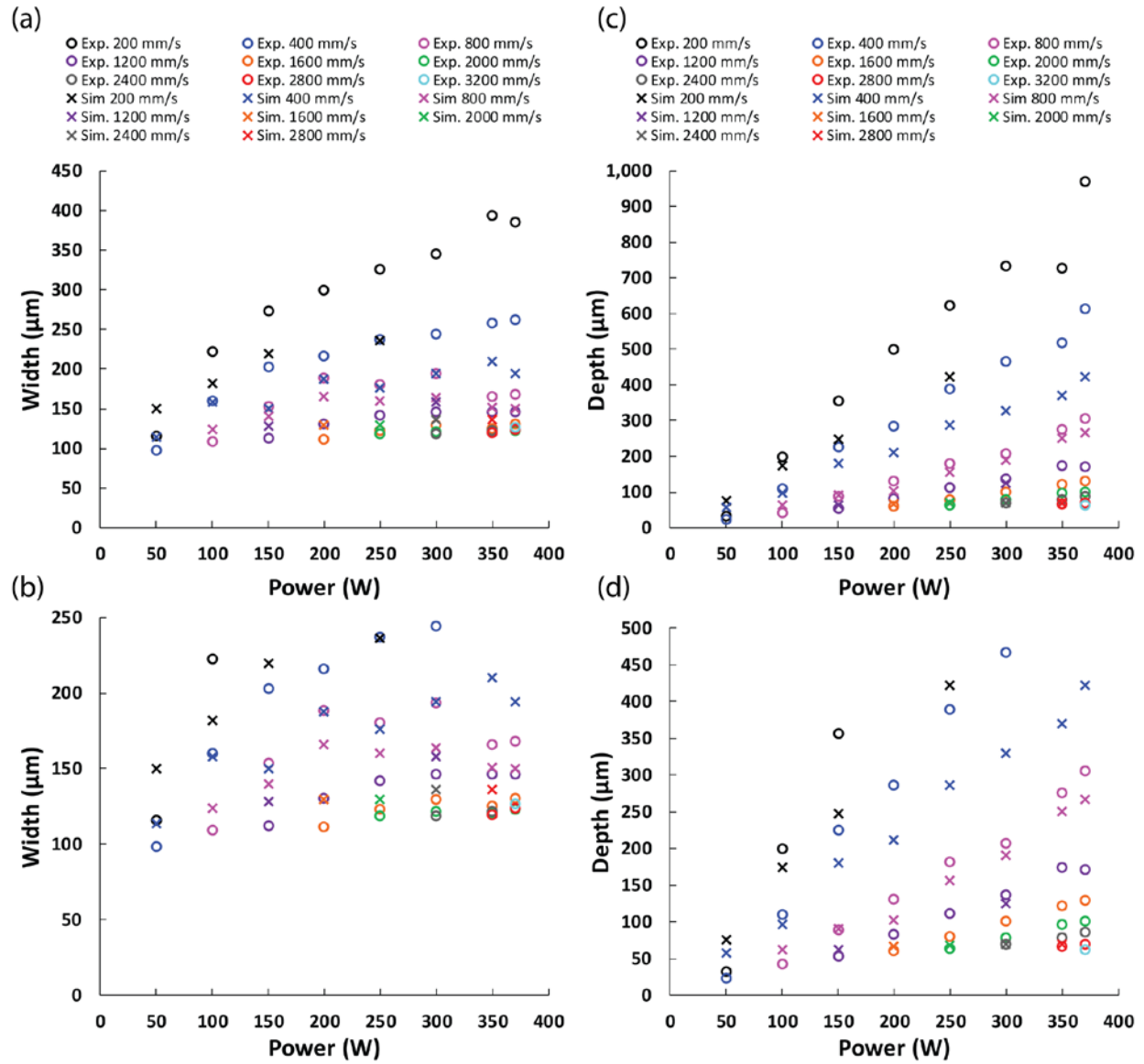


Figure A1. Melt pool width (a & b) and depth (c & d) as a function of the power for no-powder case. Simulation and experimental data are plotted with different markers. Different velocities are represented with different colors.

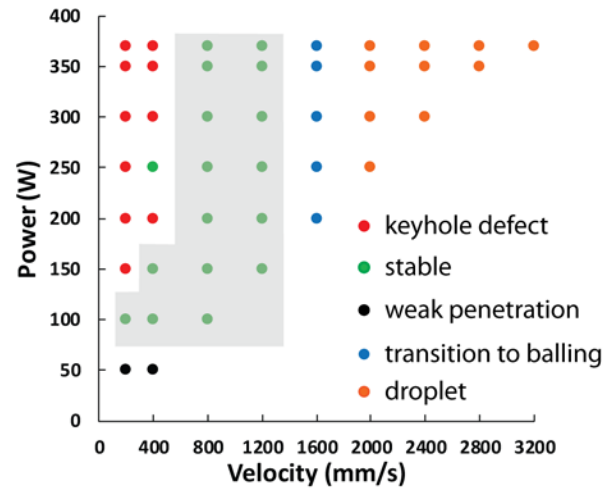


Figure A2. Single bead process map was plotted for Ti6Al4V with different colored markers. No-powder case.